PCCP

Accepted Manuscript

ROYAL SOCIETY OF CHEMISTRY

www.rsc.org/pccp

Structural Heterogeneity and Dynamics of Dyes on TiO_2: Implications for Charge Transfer across Organic-Inorganic Interfaces†

Jeffrey R. Christianson and J. R. Schmidt*

Abstract

Charge transfer across organic-inorganic interfaces plays a vital role in many important applications. Dye-semiconductor systems are the prototypical such interface and provide an excellent platform for exploring the underlying molecular-level factors that affect charge transfer dynamics and efficiency. Experiments often show multi-exponential electron injection kinetics from adsorbed dyes to a semiconductor substrate, suggesting the presence of interfacial heterogeneity. Nonetheless, both the diversity of interfacial structures and the associated implications for electronic dynamics are poorly understood. In the present work, we examine the effect of structural heterogeneity and dynamics on charge injection (as measured by dye-semiconductor electronic coupling) from plane wave density functional theory and *ab-initio* molecular dynamics calculations on model dye-semiconductor systems. We demonstrate that dye binding motif, conformation, solvation, and corresponding thermal fluctuations significantly affect charge injection kinetics. We suggest that the experimentally observed multi-exponential kinetics likely result not only from an intrinsic heterogeneous distribution of electronic coupling strengths, but also from the conformational or solvent dynamics that in turn modulate the coupling strength and/or band alignment.

1. Introduction

Efficient charge transfer across organic-inorganic interfaces is crucial for numerous materials and device applications including photo- and electro-catalysis,[1,2] molecular electronics and sensing,[3,4] and solar energy conversion.[5,6] A fundamental understanding of the factors that affect charge transfer is essential to improving efficiency and advancing practical applications, and, to this end, a plethora of studies have been carried out on such systems. Many early studies focused on densely packed, well-ordered interfaces, such as self-assembled monolayers (SAMs) on metallic substrates. Here, the commensurate lattice spacing of the underlying substrate and the molecular monolayer yields efficient, ordered packing. Consequently, SAMs comprised of tethered electron donors showed electrochemical electron injection rates that decayed exponentially with tether length, consistent with electronic tunneling.[7–12] But more generally, the *disorder* inherent to many other common organic-inorganic interfaces likely plays an important role in charge transfer kinetics. For example, Ruther *et al.* recently examined poorly-ordered monolayers on diamond (where the lattice spacings are not commensurate) and demonstrated how conformational disorder actually *enhances* electron injection, even for donors with long tethers.[13] This enhancement in the electrochemically-induced charge transfer was determined to be a result of increased through-space transfer that is facilitated by the conformational fluctuations and disorder inherent to the low-coverage systems.

Beyond thermal electron transfer, interfacial heterogeneity is also likely to affect charge transfer initiated by photoexcitation, which is important for applications in photocatalysis and solar energy conversion. For example, Grätzel and co-workers introduced dye-sensitized solar cells, in which a light-absorbing dye adsorbed to a semiconductor is photoexcited, and the resulting excited electron is injected into the conduction band of the semiconductor and through

an external circuit where it can be used to carry a load; the dye is then replenished via recombination with a suitable redox couple.[14,15] Because of the extraordinary promise for solar energy conversion that these devices have shown over the last several decades, dye-semiconductor systems have been studied extensively and therefore serve as an excellent model system to consider the effects of heterogeneity on charge transfer.

A number of factors that influence charge transfer in dye-semiconductor systems are well understood from both experimental and computational studies. Unsurprisingly, the chemical identity of the chromophore and anchoring group are of key importance. Altering the anchoring group which tethers the dye to the surface modulates the coupling between the dye and the surface, thereby affecting charge transfer.[16,17] Furthermore, multiple studies have examined the effect of changing the bridge portion of the dye that connects the anchoring group to the chromophore. Conjugated bridges facilitate increased dye-semiconductor coupling and faster injection times, while insulating bridges decrease coupling and injection rates.[18–24] If the chromophore-surface distance can be systematically controlled via the length of the insulating bridge, an exponential decrease in injection time is observed, consistent with through-space tunnelling.[7,18]

Beyond molecular identity, interfacial *heterogeneity* may also influence charge transfer kinetics.[13] The ubiquity of interfacial heterogeneity in dye-semiconductor systems is also suggested by the frequent experimental observation of multiple timescales of electron injection following photoexcitation;[18,19,25] however, less is understood regarding the impact of various sources of interfacial heterogeneity on charge injection, including variations in dye binding motif or binding site, dye conformation, solvation, as well as corresponding thermal fluctuations. This is presumably due to the difficulty of experimentally identifying and isolating the sources of

heterogeneity. In contrast, while it is challenging to fully incorporate the complexity of the experimental systems, computational modeling can isolate various forms of heterogeneity and identify their impact on charge injection.

Several prior studies have analyzed the extent and/or impact of interfacial heterogeneity on dye-semiconductor systems. For example, it is well known that there are multiple favorable binding motifs for common carboxylic acid anchoring groups on metal oxides (most commonly TiO_2).[26–29] But the vast majority of studies considering the effect of anchoring group binding on charge transfer have focused on dyes with multiple anchoring groups[30,31] and the resulting changes in orientation of rigid dyes on the surface.[32] Several studies have contrasted binding motifs of various anchoring groups[17,33] and two of the stable carboxylic acid binding motifs.[34] While the reported effects were modest, we hypothesize that other binding motifs that have not been considered previously, and in particular strong binding to oxygen vacancy sites,[28,35] could also give rise to variations in dye-semiconductor electronic coupling with corresponding impact on through-bond electron injection.

Structural heterogeneity arising from conformations of flexible dyes may also play an important role in governing injection kinetics. Introduction of insulating bridges adds a degree of conformational flexibility which may yield significantly increased dye-semiconductor coupling and injection rates versus what is expected for rigid bridges. This is the particular effect observed by Ruther *et al.* in an electrocatalytic application[13] but, as far as we are aware, has not been directly investigated for dye-semiconductor systems or photo-induced electron transfer.

Additionally, both the presence of solvent and the thermal fluctuations of the dye and solvent molecules are important contributions to the interfacial heterogeneity that may modulate charge transfer kinetics. Fluctuations in dye-substrate coupling due to nuclear motions of organic dyes have been computed using *ab-initio* molecular dynamics (AIMD),[36,37] but not in relation to conformational flexibility. Furthermore, it has been shown that solvation influences both binding motif and dye absorption spectra.[38] Since dyes are often deposited onto the semiconductor in polar solvents such as acetonitrile[19,35] and dimethyl formamide (DMF),[18] a significant number of solvent molecules likely remain adsorbed to the surface even during measurements performed under nonpolar solvents[35] or dry[18] conditions. It is well known that the adsorption of any charged or dipolar species directly affects the surface dipole, inducing a shift in the surface density of states (DOS) relative to vacuum (*i.e.*, a shift in the work function).[39–41] This effect has been noted in several computational studies, mostly concerned with water contamination of dye-semiconductor systems.[24,37,41,42] Both a significant shift (0.2 - 0.5 eV, depending on the identity of the dye)[24,37,41] and significant fluctuations in that shift (up to 0.5 eV)[24,37] due to thermal motions of the solvent have been observed for a monolayer of adsorbed water.

In the present work, we use density functional theory (DFT) and AIMD to model several recently studied Re-based dyes (see Figure 1a) tethered to a TiO_2

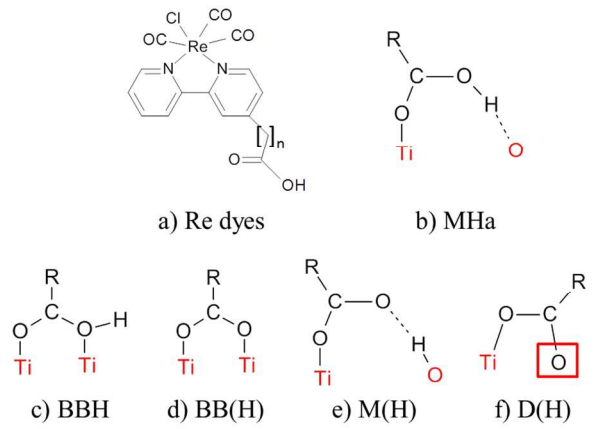

Figure 1. Re-based dyes with different bridge lengths: n = 0 (ReC), 1 (ReMeC), 2 (ReEtC) (a), and different carboxylic acid binding motifs considered: non-dissociative monodentate (b), non-dissociative bidentate (c), dissociative bidentate (d), dissociative monodentate (e), and dissociative binding to an oxygen vacancy (f).

surface. We demonstrate how interfacial structural heterogeneity arising from dye binding motif (Figure 1b-f), conformational flexibility, solvation, and thermal fluctuations has a significant effect on the extent of dye-TiO_2 electronic coupling and thus on the rate of charge injection. We make direct connections to previous experimental work on similar dye-TiO_2 systems. In particular, there have been several studies on how various bridges on ReC[19,25] and Re2C[18,43] (ReC with a second carboxylic acid anchoring group attached to the bipyridine ring) affect charge injection kinetics, as measured by transient infrared spectroscopy following the free electron absorption of the injected electron. All of these studies observed multi- or stretched-exponential injection kinetics, suggestive of interfacial heterogeneity.

Specifically, we examine the influence of various conformations with and without solvent, conformational fluctuations, binding motifs, and solvation dynamics on dye-TiO_2 coupling. We discuss the implications for both charge injection for dye-semiconductor systems and, specifically, the experimental observations of Paoprasert *et al.*[19] and Asbury *et al.*[18] Since dye-semiconductor systems serve as an excellent model for other applications involving interfacial charge transfer, we anticipate that many of these conclusions will be transferable to related organic-inorganic interfaces.[36]

2. Methods

All calculations were performed using the Vienna Ab-initio Simulation Package (VASP)[44–47] using the Perdew-Burke-Ernzerhof (PBE) GGA exchange-correlation functional[48,49] and the projector augmented wave (PAW) method[50,51] for describing the interaction between core electrons and valence electrons (including the 3p electrons on Ti). Unless otherwise noted, all calculations were run with an energy cutoff of 400 eV, normal precision, 0.05 eV Gaussian smearing, no spin polarization, and a dipole correction orthogonal to the TiO_2 slab interface.

Because of the large size of the supercell used, the Brillouin zone was only sampled at the gamma point for optimizations, while a denser 5 × 5 × 1 Monkhorst-Pack grid used to more accurately represent the density of states. Although pure GGA functionals are well known to underestimate band gaps for both semiconductor and dye systems, the predicted band alignment for the dye lowest unoccupied molecular orbital (LUMO) and TiO_2 conduction band are qualitatively correct. Furthermore, we are focused primarily on qualitative *trends* within a related series of dyes which should lead to cancellation of many systematic DFT errors. Additionally, while inadequacies of DFT in describing dispersion interactions will affect dye binding energies, trends in electronic dye-surface coupling should be described well.

Visualizations of the periodic systems were prepared using VMD.[52] All geometrical manipulations of the model system were performed using the Atomistic Simulation Environment (ASE).[53] The TiO_2 anatase (101) surface was generated from experimental bulk anatase lattice parameters (a = 3.7845 Å, c = 9.5143 Å),[54] and the slab model was a 1 × 3 supercell consisting of 24 TiO_2 units (two layers of Ti atoms) and spanning 10.24 and 11.35 Å in the x- and y-directions, respectively. The dye molecule was then adsorbed to the surface in a geometry corresponding to one of several considered binding motifs. For the largest dye considered (ReEtC), adsorption onto this TiO_2 supercell resulted in a distance between periodic images of the bipyridine ring of approximately 7 Å (4 Å) for the upright (bent) configuration, and thus we anticipate a minimal influence of adsorbate-adsorbate interactions on injection rates. After adsorption of the dye molecule, a vacuum gap of about 10 Å was added in the z-direction to minimize interactions with periodic images; the total length of the unit cell in the z-direction was then approximately 30 Å, depending slightly on the identity of the dye molecule. For cases where bulk explicit solvent was considered (Figure 2), solvent molecules were then added to the

box without overlap with TiO_2 or dye atoms and in number consistent with the room temperature density of the solvent and the approximate volume not occupied by the dye or TiO_2 slab. Geometries for monolayer coverage were formed by removing solvent molecules not adsorbed to either surface from an equilibrated bulk solvation configuration.

Geometry optimizations were then performed holding the bottom half of the anatase slab fixed in bulk positions. For dye-TiO_2 systems (no solvent), this was done using ASE, first to loose convergence with the FIRE optimizer[55] and then to a maximum force less than 0.05 eV/Å with LBFGS. Single points along the geometry optimization were run in VASP (interfaced with ASE) using an energy cutoff of 300 eV and low precision. For systems with explicit solvent molecules, geometry optimizations were run solely in VASP (400 eV energy cutoff and normal precision)

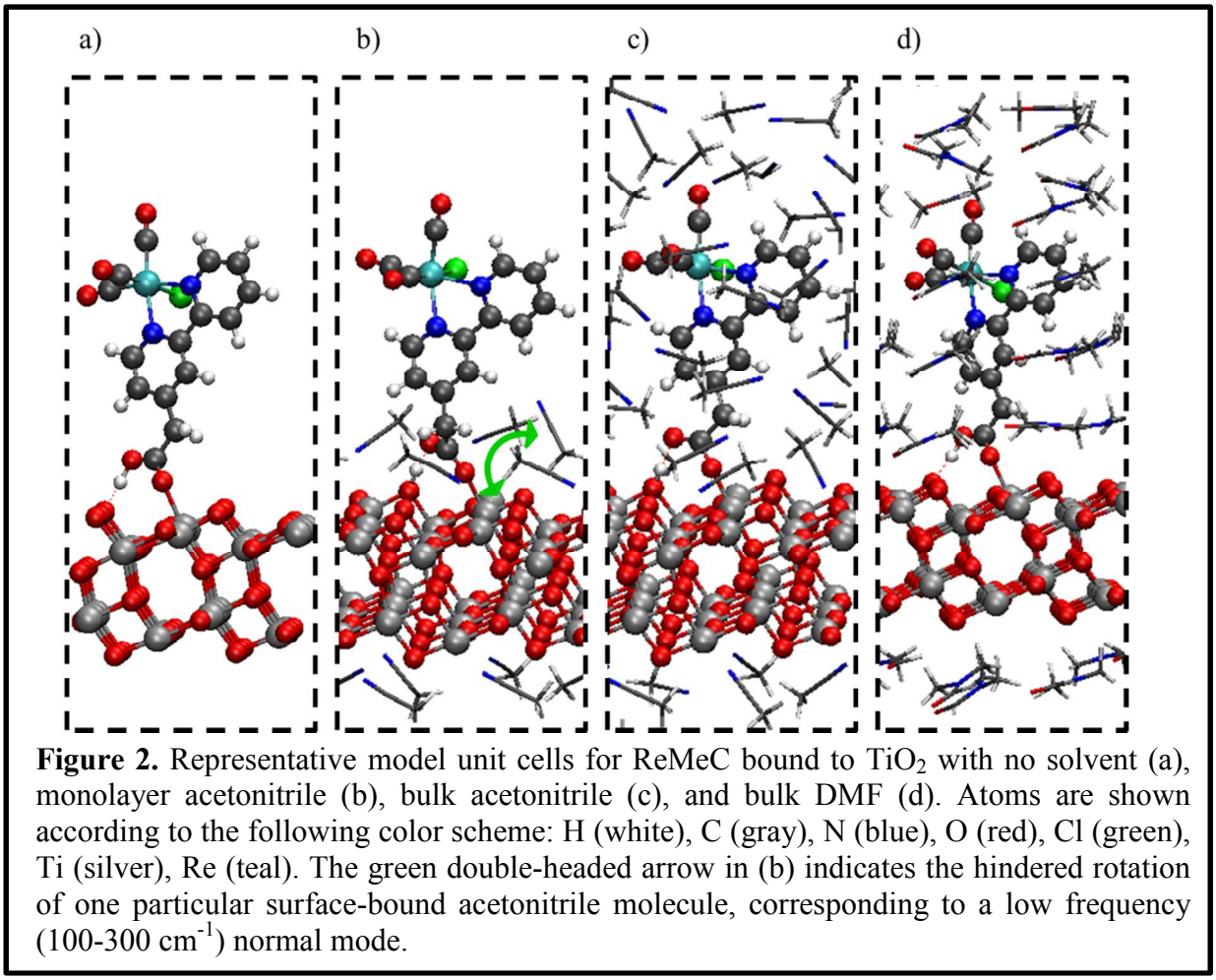

Figure 2. Representative model unit cells for ReMeC bound to TiO_2 with no solvent (a), monolayer acetonitrile (b), bulk acetonitrile (c), and bulk DMF (d). Atoms are shown according to the following color scheme: H (white), C (gray), N (blue), O (red), Cl (green), Ti (silver), Re (teal). The green double-headed arrow in (b) indicates the hindered rotation of one particular surface-bound acetonitrile molecule, corresponding to a low frequency (100-300 cm^{-1}) normal mode.

using its conjugate gradient method for loose convergence and RMM-DIIS for convergence to a maximum force less than 0.05 eV/Å.

AIMD was carried out by propagating the nuclei classically according to Newton's equations of motion using a Verlet algorithm and a 1 fs time step. The MD was done in the NVT ensemble, and a temperature of 300 K was enforced by an Andersen thermostat with a collision probability of 0.002 fs^{-1} for each atom. The system was equilibrated at 300 K (generally for several hundred fs) prior to data collection.

Coupling of the dye *excited state* to the surface conduction band governs the timescale for electron injection. However, for computational feasibility, we assume that the strength of the electronic coupling of the dye *ground state LUMO* to the TiO_2 conduction band states provides a qualitative estimate of injection time, and we estimate this coupling using the Newns-Anderson model of chemisorption,[56,57] as has been done previously for similar dye-TiO_2 systems.[21,31] Within the model, the density of dye LUMO states, $\rho_{LUMO}(E)$, is described by a Lorentzian

$$\rho_{LUMO}(E) = \frac{1}{\pi}\frac{\Delta}{\left(E - E_{LUMO}(ads)\right)^2 + \Delta^2},$$

where $E_{LUMO}(ads)$ is the energy of the isolated adsorbate's LUMO (assumed to be the center of the peak for the adsorbate-surface system). The full width at half of the maximum (FWHM) density, 2Δ, is interpreted as a lifetime broadening (LB), is related to the dye LUMO - TiO_2 coupling weighted by the DOS, and gives an estimation of the electron transfer time, τ:

$$\tau = \frac{\hbar}{2\Delta}.$$

Thus, a direct estimate for the electron injection rate (dependent on the electronic coupling of the dye LUMO to the TiO_2 conduction band) can be obtained from a projected density of states (PDOS) of the dye-TiO_2 system. While this is certainly a crude approximation for injection rates,

it allows for both analysis of the *trends* in injection rates[31] and *qualitative* comparisons to experiments.[21] We follow the procedure set forth by Persson *et al.*[21] with three modifications. First, because we use a plane wave basis, we project each dye-TiO_2 virtual band into a small atomic basis set (see ESI†) using a projection scheme[58] and use this to obtain the dye PDOS. Second, because the dye LUMO is not delocalized over the bridge atoms, we only sum over the bipyridine, carbonyl, Re, and Cl atoms to obtain the PDOS of the LUMO. The PDOS over the energy interval generally summed to one orbital within several percent and was then normalized to one in order to ensure accurate evaluation of the peak center, E_{LUMO}(ads). Third, the FWHM was obtained more precisely. Previously, the mean deviation of the distribution was used.[21,31] However, this quantity is not well defined for a Lorentzian distribution, since the corresponding integral diverges. Given various test distributions, this method for calculating the FWHM produced errors of up to 20%.[21] However, the "half moment" of a Lorentzian distribution *is* defined and is related to the FWHM (2Δ). So, in the context of the Newns-Anderson model,

$$\frac{1}{\pi}\int \frac{\Delta\sqrt{E - E_{LUMO}}}{\left(E - E_{LUMO}(ads)\right)^2 + \Delta^2} dE = \sqrt{2\Delta}.$$

Therefore, the FWHM was calculated from the PDOS using the following:

$$2\Delta = \left[\frac{1}{N_k}\sum_i p_i\sqrt{E_i - E_{LUMO}(ads)}\right]^2,$$

where N_k is the number of irreducible *k* points (13, as generated from a 5 × 5 × 1 Monkhorst-Pack grid), the sum runs over all bands surrounding the dye LUMO, p_i is the proportion of band *i* localized on the dye atoms listed above, and E_{LUMO}(ads) is calculated as before.[21]

The PDOS as computed by VASP was used to estimate E_{LUMO} - E_{CBM}, the position of the dye LUMO relative to the TiO_2 conduction band minimum (CBM) in solvent.

3. Results and Discussion

Dye conformation and binding motif. The Re-based dyes with various bridge lengths are shown in Figure 1a, and the different carboxylic acid binding motifs that we consider are shown in Figure 1b-f. These are the same binding motifs that we considered previously[35] and are analogous to the most stable binding modes of formic acid to anatase.[29] Significant increases in the lifetime broadening (LB) of the dye LUMO, indicative of stronger dye-surface electronic coupling, occur with decreasing bridge length (Table 1). This trend is already well understood on the basis of prior experimental[7,18,19] and computational[21–23] studies as an insulating effect; direct conjugation of the dye to the surface increases through-bond electronic coupling, whereas insulating groups separating the chromophore from the surface exponentially decrease through-space electronic coupling as a function of bridge length. We note that we observe the same qualitative trend in going from ReC to ReMeC to ReEtC as Asbury *et al.*[18] observe in the two-anchor analogs going from Re2C to Re2MeC to Re2PrC, and our predicted rapid injection time for ReC (5 fs) is consistent with both Paopasert *et al.*[19] (< 250 fs) and Asbury *et al.* (< 100 fs for Re2C). (Note that in the case of ReC, the assumption of non-adiabatic electronic transfer, inherent in the estimation of injection time from the Newns-Anderson model, may be violated due to the strength of the electronic coupling.) However, we find qualitative differences in the absolute predicted injection time for ReMeC (240 fs) as compared to that observed for Re2MeC (19 ps); the discrepancy appears to be due to neglect of solvation effects, as discussed in detail below.

Table 1. Effect of Bridge Length and Defect Adsorption on Dye LUMO LB (meV)[a]

	ReC	ReMeC	ReEtC
MHa	120	2.8	0.4
D(H)	140	6.6	0.9

[a]Re-based dyes with alkyl bridges with 0 (ReC), 1 (ReMeC), and 2 (ReEtC) carbon atoms are schematically shown in Figure 1a. Non-dissociative monodentate (MHa) and dissociative defect (D(H)) binding motifs are depicted in Figure 1b and f, respectively.

We also examine the influence of binding motif on electronic coupling strength. These differences are particularly relevant in that there are several comparable stable binding motifs for carboxylic acids on anatase TiO_2.[26–29] Interestingly, we find that the LB is increased upon binding to an oxygen vacancy (Table 1) but is otherwise rather insensitive to binding motif; for the ReMeC dye binding in MHa, M(H), BBH, and BB(H) geometries, the LB is 3.1 (± 0.5) meV. Previously, it has been reported that dissociated versus non-dissociated binding of carboxylic acids has a small to moderate effect on injection times, depending on the dye.[34] However, the effect of binding to defect sites has not been considered. Our results indicate that binding to defect sites leads to an increased through-bond electronic coupling yielding a higher LB. For all three dyes, the same basic dye configuration (standing upright) was preserved for all binding motifs, resulting in very similar distances between the bipyridine ring and the surface (changes of only several tenths of an angstrom). Thus, the differences observed for binding to an oxygen vacancy must be the result of increased through-bond coupling. This is consistent with the relative adsorption energies of the different binding motifs. As we have shown recently,[35] the adsorption energy of ReC binding to an oxygen vacancy is much stronger than when binding in any of the other energetically favorable motifs (-2.4 versus approximately -1.2 eV). This much stronger dye-TiO_2 adsorption interaction is most likely the cause of the increased electronic coupling noted here. While there is still very recent debate over whether[28] or not[27] there is direct experimental evidence for carboxylic acid binding to oxygen vacancies (due to differences in TiO_2 surface preparation and in interpretation of the IR spectra), it is likely that some oxygen vacancies are present at the surface of the nanoparticles most frequently used for such dye-TiO_2 studies.[59–61] Some fraction of these sites will likely be passivated by adsorbed dyes, while others

adsorb on more abundant terrace sites. As indicated by our results (Table 1), this heterogeneity could lead to injection rates that differ by up to a factor of two to three. However, due to the relative invariance of coupling strength among the remaining (non-defect) binding motifs, the MHa binding motif is used for the rest of the results as representative of non-defect binding, since this corresponds to the most stable binding motif for ReC.[35]

While binding motif modulates through-bond coupling, increasing bridge length allows for increased conformational flexibility and corresponding changes in through-space dye-TiO_2 electronic coupling. The timescale for these large conformation changes are long compared to the lengths of typical AIMD simulations; thus we instead examine several representative examples. Rotation around the dihedral angles in the ethyl bridge of ReEtC allows for shorter distances between the bipyridine ring and the TiO_2 surface, which increases the LB of the dye LUMO from 0.4 to 5.5 meV (Figure 3). Since the binding motif was kept constant for the two conformations, the difference in coupling likely arises from differences in through-space coupling. It is clear that both chain length and flexibility must be considered in determining the effect of the bridge on charge injection, with the observed coupling strengths spanning an order of magnitude. If the bridge is rigid[18] or if a well-ordered, high-coverage monolayer is achieved,[62] then an exponential decay of injection rate as a function of insulating chain length may be expected.[7,18] In other cases, however, the flexibility of the

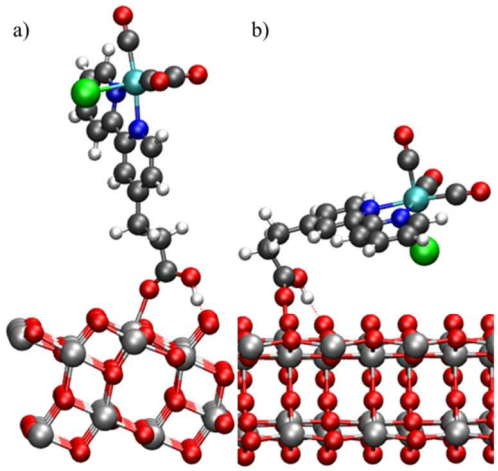

Figure 3. Conformational flexibility of ReEtC: standing up, LB = 0.4 meV (a) and bent, LB = 5.5 meV (b). Atoms are shown according to the following color scheme: H (white), C (gray), N (blue), O (red), Cl (green), Ti (silver), Re (teal).

chain adds to the heterogeneity of both the surface and the injection rates. This principle is consistent with the findings of Ruther *et al.* for thermal electron transfer, who concluded that in the absence of dynamic crowding effects on the surface, conformational flexibility allows for improved through-space electron transfer.[13] It also highlights the potentially important role of dye coverage and packing on charge injection efficiency.[35,62]

This principle is also reflected in the recent results of Asbury *et al.*[18] and Paoprasert *et al.*[19] The former examined dyes with two anchoring groups, which are thus extremely rigid and cannot access conformations with the bipyridine ring close to the surface. As such, those authors observed an exponential decay of injection rate with increasing bridge length from Re2MeC (19 ps) to Re2PrC (240 ps). In contrast, Paoprasert *et al.* employed dyes with only a single anchoring group, yielding significant conformational flexibility. Multiple injection rates were observed for all dyes considered, and although the slowest timescale was an order of magnitude slower for the insulating bridge than for the conjugated bridge, the fastest timescale was < 250 fs for all dyes. The insulating methyl propionate based bridge is very flexible and is able to rotate about several dihedral angles. Based on the role of flexibility that we observe in ReEtC, it seems likely that the flexibility of the insulating bridge is responsible for the extremely fast observed timescale.

Our results also highlight the possibility for the direct experimental identification of various dye conformations by vibrational spectroscopy by probing the ligand carbonyl stretches of the Re chromophore. We have previously shown that the completely symmetric carbonyl stretch is largely independent of ReC conformation, and that the experimentally observed vibrational spectroscopic heterogeneity is primarily a result of vibrational coupling within dye aggregates.[35] However, in the case considered here, the conformational flexibility of ReEtC allows for both shorter chromophore-surface and carbonyl-surface contacts. In order to determine if the upright

and bent conformations could be distinguished spectroscopically, we carry out vibrational frequency calculations at lower dye coverage (to eliminate potential vibrational coupling; the shortest distance between any carbonyl atom and any dye atom from its periodic images was at least 5.5 Å), consistent with the methodology described previously.[35] For configurations analogous to those depicted in Figure 3, we observe very little (less than 2 cm^{-1}) difference in the vibrational frequencies of the carbonyl stretching modes between the two conformations, since the carbonyl ligands are still appreciably far from the surface in Figure 3b (at least 6 Å). We also consider the case where the axial carbonyl and Cl ligands are exchanged such that the axial carbonyl ligand points toward the surface, corresponding to a bending of the ethyl bridge in the opposite direction. In this case, the *asymmetric* stretch (where the stretch of the axial carbonyl ligand is out of phase with the stretches of the equatorial carbonyl ligands) decreases from 1921 to 1908 cm^{-1} upon bending of the ReEtC dye. This indicates that spectroscopic identification of some of the bent configurations may be possible by carefully controlling for dye aggregation and observing the *asymmetric* stretching region.

Solvation. Solvent induces additional important sources of heterogeneity, with implications for electronic coupling and injection. Although this is not unexpected based on simple Marcus theory-type arguments,[63,64] note that, additionally, the significant anisotropy induced by the planar semiconductor interface can cause significant shifts of the relative donor and acceptor levels in polar solvents. Including explicit solvent molecules in the unit cell affects the LB of the dye LUMO by shifting its position relative to the TiO_2 conduction band. While this substantial shift for monolayer coverage (0.8 - 1.5 eV) has been noted previously and attributed to dipolar interactions of the solvent adsorbed to the surface,[41,65] the effect on dye-TiO_2 electronic coupling has not been thoroughly investigated. For an optimized solvent (acetonitrile) configuration

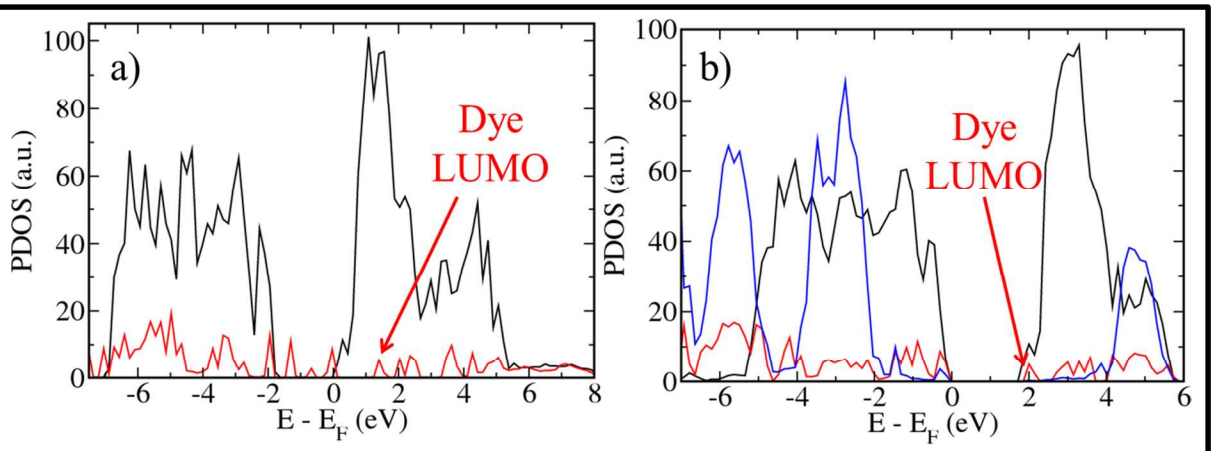

Figure 4. PDOS for ReMeC bound to TiO_2 with no solvent (a), and with explicit acetonitrile (b). Contributions are shown from TiO_2 (black), ReMeC (red), and acetonitrile (blue).

around the ReMeC dye, the dye LUMO is shifted to a region of low TiO_2 DOS (Figure 4), and the LB decreases from 2.8 meV to < 1 meV. A qualitatively similar shift is observed both for explicit DMF solvation and for monolayer coverage of acetonitrile on the surface. Additionally, an analogous LB decrease from 120 to 30 meV is observed for ReC solvated by acetonitrile. Although the ReC LUMO (localized on the bipyridine) is directly conjugated to the surface via the carboxylic acid anchoring group, this can still be understood as arising from the same phenomenon as for ReMeC: the ReC LUMO shifts to a region of low TiO_2 DOS (near the CBM), and the net electronic coupling therefore decreases. However, the direct conjugation to the surface still allows for significant residual coupling.

This solvent effect also explains the qualitative discrepancy mentioned above between our estimated injection rate for ReMeC without solvent and the rate for Re2MeC observed by Asbury *et al.*,[18] who prepared the dye-sensitized films in DMF. Whereas with no solvent we observe a LB of 2.8 meV (corresponding to a timescale for injection of ~240 fs), the shift of the dye LUMO relative to the TiO_2 CBM induced by the solvent results in coupling weaker than our ability to resolve (corresponding to a timescale of > 1 ps) and is qualitatively consistent with the experimentally observed timescale of 19 ps. When accounting for solvent in the case of ReC, the

decrease in LB to 30 meV (injection time of 22 fs) remains consistent with the rapid injection observed by both Asbury *et al.* (< 100 fs for Re2C) and Paoprasert *et al.* (< 250 fs).[19]

Thermal fluctuations. Analysis of static local minima provides important insight into the effect of structural heterogeneity on dye-surface electronic coupling. However, heterogeneity induced by thermal (conformational or solvent) fluctuations may also play a significant role in modulating electron injection kinetics. Results from 5 ps of AIMD sampling of ReEtC without solvent in a bent configuration where the bipyridine is close to the surface are shown in Figure 5. Here, given computational restrictions, AIMD is used to sample *fluctuations* of the dye within a given conformational basin, while the influence of large-scale conformation changes were addressed above. Even within this single conformation, LBs of 5-10 meV are common, but conformational fluctuations can give rise to LBs as high as 60 meV. (Note that a better description of dispersion interactions may increase the likelihood of these higher LB configurations by favoring conformations with closer dye-surface contacts.) Based on anaylsis of the underyling trajectory, these fluctuations in LB are mostly due to corresponding fluctuations in the bipyridine-surface distance; shorter distances generally yield stronger dye-TiO_2 coupling and therefore higher LBs. While other factors may also be important (such as orientation of the bipyridine ring in relation to the quality of orbital overlap with the surface), the average distance of the bipyridine heavy atoms from the surface correlates well with the calculated LB (see ESI†).

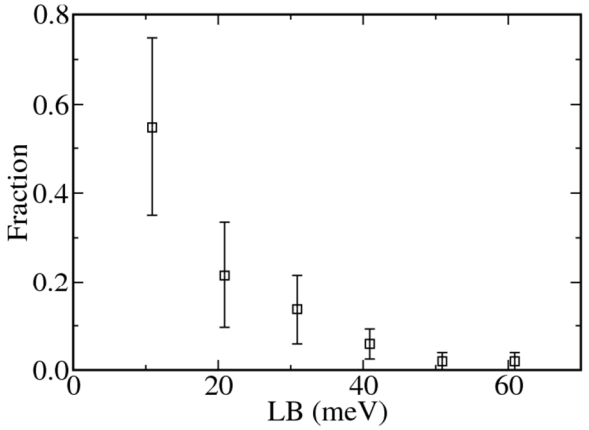

Figure 5. Distribution of LB for 50 geometries along the AIMD trajectory sampling bent ReEtC configurations. Statistical uncertainties shown are from block averaging.

Thus, thermal fluctuations within a particular local minimum can also alter the LB (and therefore the injection time) by an order of magnitude.

We also consider thermal fluctuations of the solvent. Since the effect of the solvent appears to be mainly due to the relative shift of the TiO_2 conduction band, we consider the distribution of dye LUMO positions relative to the TiO_2 CBM (E_{LUMO} - E_{CBM}) arising from thermal fluctuations. The distributions obtained from AIMD trajectories of ReMeC solvated by bulk and monolayer acetonitrile and bulk DMF are shown in Figure 6. In all cases, large fluctuations are observed giving rise to Gaussian distributions with FWHMs of approximately 0.6 eV and centered at various positions below the TiO_2 CBM. The similarity between acetonitrile (centered at -0.4 eV) and DMF solvated dye (centered at -0.6 eV) is expected because of their nearly identical dipole moments (3.9 D). The monolayer acetonitrile system indicates that the shift is largely caused by solvent adsorption to the surface; the center of the distribution lies at approximately -0.1 eV relative to the CBM, whereas the dye LUMO in the absence of solvent lies 1.4 eV above the CBM (see Figure 4a). This shift of 1.5 eV is consistent with the range of shifts found previously (0.8-1.5 eV) for monolayer acetonitrile coverage for several dyes.[41] Nevertheless, bulk solvation (*i.e.*, additional layers of solvent) does modestly increase the shift

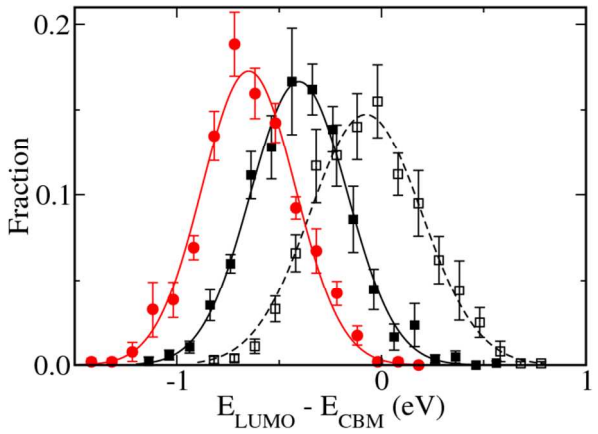

Figure 6. Distributions (points) of E_{LUMO} - E_{CBM} for geometries along AIMD trajectories fit to Gaussians (lines) for bulk-solvated acetonitrile (closed black squares and solid black line), monolayer acetonitrile (open black squares and dashed black line), and bulk-solvated DMF (closed red circles and solid red line). Statistical uncertainties shown are from block averaging.

further so that the distribution is centered at -0.4 eV. In any case, the relative shift of the CBM to the dye LUMO due to the solvent results in a majority of configurations where the dye LUMO lies either below the CBM or in a region of low density of TiO_2 conduction band states, which yields a much smaller electronic coupling than estimated with no solvent.

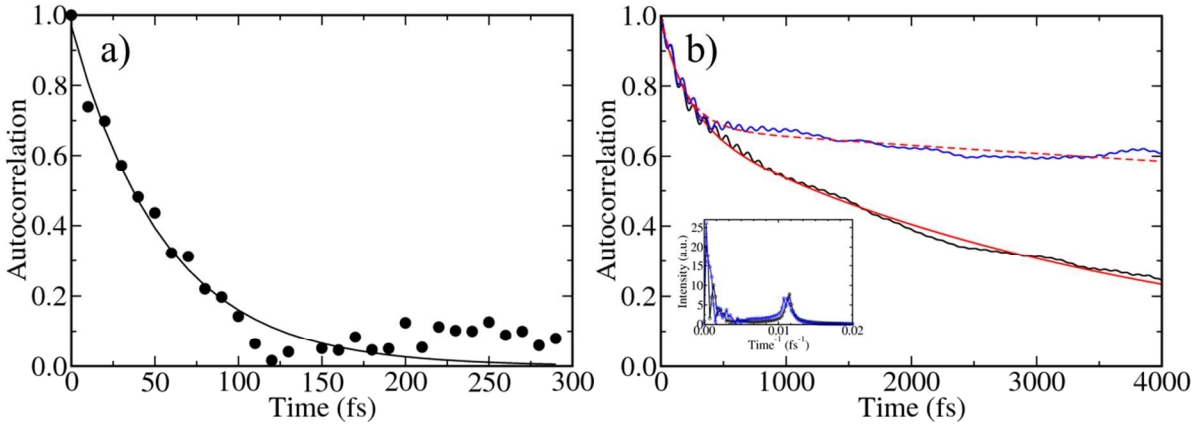

Figure 7. Autocorrelation function (black points) for the relative shift of the ReMeC LUMO in acetonitrile fit (black line) to an exponential decay (a) and rotational autocorrelation functions of solvent, *C*(t), fit to bi-exponential decays for the bulk (black points and solid red line) and monolayer (blue points and dashed red line) acetonitrile molecular dipole rotation (b). The inset in (b) shows the Fourier transforms of the difference of the autocorrelation function in (b) and its bi-exponential fit for both bulk (black) and monolayer (blue) acetonitrile.

In order to identify the cause of the large fluctuations in E_{LUMO} - E_{CBM}, we examine the time scale of the fluctuations as well as the timescale of solvent rotations (the latter is correlated with changes in the net surface dipole). The autocorrelation function of the relative dye LUMO positions for bulk solvation by acetonitrile is shown in Figure 7a and decays exponentially with a time constant of 56 fs. A very similar decay is observed for DMF (54 fs) and a modestly longer decay (110 fs) is observed for monolayer acetonitrile solvation (see ESI†). For comparison, the rotational autocorrelation functions of acetonitrile molecular dipoles were obtained by monitoring the time evolution of the C-N unit vector of each molecule to obtain the rotational autocorrelation:[66]

$$C(t) = \langle P_2(t) \rangle = \frac{1}{2} \langle 3cos^2\big(\theta(t)\big) - 1 \rangle$$

where $\theta(t) = \boldsymbol{\mu}(0) \cdot \boldsymbol{\mu}(t)$, and $\boldsymbol{\mu}$ is the molecular C-N unit vector. Thus, for each configuration from the AIMD trajectory, $\boldsymbol{\mu}$ was obtained for each acetonitrile molecule, and the autocorrelation function at each time point represents an average over both solvent molecules and time steps. These autocorrelation functions for bulk and monolayer acetonitrile are shown in Figure 7b and exhibit multi-exponential decays. Good fits are obtained to bi-exponential decays with fast (230 fs for bulk and 180 fs for monolayer) and slow (4 ps for bulk and 27 ps for monolayer) components. Yet even the fast components are too long to correspond to the timescales of E_{LUMO} - E_{CBM} fluctuations. However, the periods of the oscillations overlaying the exponential decays are approximately 85-90 fs (see inset in Figure 7b). This timescale lies between the timescales observed for bulk (56 fs) and monolayer (110 fs) solvation. Visual analysis of the trajectory indicates that these fluctuations correspond to a wagging motion (or hindered rotation) of individual *surface-bound* acetonitrile molecules (see Figure 2b). This motion corresponds to low-frequency normal modes of total system, wagging of the adsorbed molecules coupling to surface phonons. We therefore attribute the large fluctuations in E_{LUMO} - E_{CBM} to the wagging of the associated molecular dipoles.

While a shift in the TiO_2 conduction band due to acetonitrile adsorption has been noted previously,[41] the large fluctuations of this shift due to thermal motions of the solvent molecules have not been noted and have implications for charge injection kinetics. While the timescale for these large fluctuations appear to be relatively fast (< 100 fs), the large shift indicates that (in this case) many configurations result in zero to very weak electronic coupling. The importance of these fluctuations will depend crucially on the *average* solvent-induced shift of the donor relative to the semiconductor CBM. In an extreme case, where the solvent has pushed the average donor

level well into the semiconductor bandgap, the dye must wait for relatively rare solvent fluctuations yielding significant coupling prior to charge injection. Since the timescale for such a rare fluctuation may be significantly longer than that of the actual electron transfer event itself, one may (in such a case) envision a transition into a solvent-driven Marcus theory picture where the timescales governing electron injection may be much slower than suggested by the electronic coupling strength estimated from calculations without solvent.[63,64] In cases where the solvated donor level remains well within the semiconductor conduction band and/or the dye-semiconductor coupling is particularly strong (such as for dyes with conjugated linkers), the direct influence of solvent on electron transfer will be less significant.

4. Conclusions

Our results clearly indicate that interfacial structural heterogeneity significantly affects dye-semiconductor electronic coupling, with a concomitant influence on injection rates. In particular, heterogeneity arising from binding motif, conformational flexibility, and the presence of solvent all influence the extent of the electronic coupling. Binding to defect sites increases through-bond coupling, while conformational flexibility provided by insulating bridges may allow for dramatic fluctuations in the resulting through-space coupling. In contrast, solvent modifies dye-TiO_2 electronic coupling indirectly by changing the band alignment and therefore the number of TiO_2 conduction band states to which the dye can couple. Beyond static heterogeneity, thermal fluctuations also give rise to significant modulation in dye-TiO_2 coupling. Thermal fluctuations of the dye, even within a given conformation, lead to changes in dye-substrate coupling spanning an order of magnitude, whereas thermal fluctuations of the surface-adsorbed solvent change the extent of band shifting.

The impact of conformational and thermal fluctuations on injection will also depend crucially on the timescale of these processes.[67–69] The intrinsic timescale for electron injection (the shortest timescale observed experimentally) is approximately 0.1 ps. Fluctuations much more rapid than this characteristic injection time will be averaged out (yielding simple single-exponential behavior), while slower fluctuations will give rise to multi-exponential kinetics.[67] The large-scale conformational transformations discussed in this contribution certainly fall into the latter category. In contrast, the timescales for the thermal (solvent or dye) fluctuations considered here using AIMD are on the same order of magnitude as the characteristic injection time. In the regime where the dye LUMO lies well within the TiO_2 conduction band, these fluctuations may be largely averaged out. However, when the dye LUMO lies in the band gap (which is the case for the dyes studied here in the presence of solvent), rare thermal fluctuations are needed to give rise to bring donor and acceptor states into resonance and yield coupling strong enough for electron transfer. In this regime, analogous to Marcus theory of molecular electron transfer, although the fluctuations themselves are relatively fast, the probability of an effective fluctuation giving rise to electron transfer is low. In such a case, multi-exponential kinetics may arise from timescales of the various *fluctuations* (followed by *rapid* injection), rather than intrinsic heterogeneity in the *injection* process itself.

In summary, our results suggest that the multi-exponential injection kinetics observed in experiments reflect a variety of factors, including not only variations in the inherent electron injection dynamics due to static structural heterogeneity, but also the timescales of associated conformational and solvent dynamics that lead to strong coupling and injection. We anticipate that these conclusions are largely transferable to other systems where understanding the effect of

interfacial heterogeneity on efficient charge transfer is crucial, such as photo- and electro-catalysis and molecular electronics.

Acknowledgements

The authors gratefully acknowledge primary support of this research and use of computational facilities by the University of Wisconsin Materials Research Science and Engineering Center (DMR-1121288). Additional computational resources were provided by National Science Foundation Grant CHE-0840494. J.R.S. is an Alfred P. Sloan Research Fellow and a Camille Dreyfus Teacher-Scholar. The authors also thank Benjamin Dunnington for providing a customized version of the code used for projecting virtual bands onto an atomic-centered basis set.

References

1. D. L. Ashford, W. Song, J. J. Concepcion, C. R. K. Glasson, M. K. Brennaman, M. R. Norris, Z. Fang, J. L. Templeton, and T. J. Meyer, *J. Am. Chem. Soc.*, 2012, **134**, 19189–19198.

2. A. K. Vannucci, Z. Chen, J. J. Concepcion, and T. J. Meyer, *ACS Catal.*, 2012, **2**, 716–719.

3. A. Heller, *J. Phys. Chem.*, 1992, **96**, 3579–3587.

4. K. J. Albert, N. S. Lewis, C. L. Schauer, G. A. Sotzing, S. E. Stitzel, T. P. Vaid, and D. R. Walt, *Chem. Rev.*, 2000, **100**, 2595–2626.

5. J. B. Asbury, E. Hao, Y. Wang, H. N. Ghosh, and T. Lian, *J. Phys. Chem. B*, 2001, **105**, 4545–4557.

6. N. Robertson, *Angew. Chem. Int. Ed. Engl.*, 2006, **45**, 2338–2345.

7. J. F. Smalley, S. W. Feldberg, C. E. D. Chidsey, M. R. Linford, M. D. Newton, and Y.-P. Liu, *J. Phys. Chem.*, 1995, **99**, 13141–13149.

8. M. D. Porter, T. B. Bright, D. L. Allara, and C. E. D. Chidsey, *J. Am. Chem. Soc.*, 1987, **109**, 3559–3568.

9. C. E. D. Chidsey, C. R. Bertozzi, T. M. Putvinski, and A. M. Mujsce, *J. Am. Chem. Soc.*, 1990, **112**, 4301–4306.

10. C. E. Chidsey, *Science*, 1991, **251**, 919–922.

11. H. O. Finklea and D. D. Hanshew, *J. Am. Chem. Soc.*, 1992, **114**, 3173–3181.

12. S. Creager, C. J. Yu, C. Bamdad, S. O'Connor, T. MacLean, E. Lam, Y. Chong, G. T. Olsen, J. Luo, M. Gozin, and J. F. Kayyem, *J. Am. Chem. Soc.*, 1999, **121**, 1059–1064.

13. R. E. Ruther, Q. Cui, and R. J. Hamers, *J. Am. Chem. Soc.*, 2013, **135**, 5751–5761.

14. B. O'Regan and M. Gratzel, *Nature*, 1991, **353**, 737–740.

15. M. K. Nazeeruddin, A. Kay, I. Rodicio, R. Humphry-Baker, E. Mueller, P. Liska, N. Vlachopoulos, and M. Gratzel, *J. Am. Chem. Soc.*, 1993, **115**, 6382–6390.

16. C. She, J. Guo, S. Irle, K. Morokuma, D. L. Mohler, H. Zabri, F. Odobel, K.-T. Youm, F. Liu, J. T. Hupp, and T. Lian, *J. Phys. Chem. A*, 2007, **111**, 6832–6842.

17. F. Ambrosio, N. Martsinovich, and A. Troisi, *J. Phys. Chem. Lett.*, 2012, **3**, 1531–1535.

18. J. B. Asbury, E. Hao, Y. Wang, and T. Lian, *J. Phys. Chem. B*, 2000, **104**, 11957–11964.

19. P. Paoprasert, J. E. Laaser, W. Xiong, R. A. Franking, R. J. Hamers, M. T. Zanni, J. R. Schmidt, and P. Gopalan, *J. Phys. Chem. C*, 2010, **114**, 9898–9907.

20. T. Dos Santos, A. Morandeira, S. Koops, A. J. Mozer, G. Tsekouras, Y. Dong, P. Wagner, G. Wallace, J. C. Earles, K. C. Gordon, D. Officer, and J. R. Durrant, *J. Phys. Chem. C*, 2010, **114**, 3276–3279.

21. P. Persson, M. J. Lundqvist, R. Ernstorfer, W. A. Goddard, and F. Willig, *J. Chem. Theory Comput.*, 2006, **2**, 441–451.

22. F. De Angelis, *Chem. Phys. Lett.*, 2010, **493**, 323–327.

23. R. Sánchez-de-Armas, J. Oviedo, M. A. San Miguel, and J. F. Sanz, *J. Phys. Chem. C*, 2011, **115**, 11293–11301.

24. S. Manzhos, H. Segawa, and K. Yamashita, *Phys. Chem. Chem. Phys.*, 2012, **14**, 1749–1755.

25. W. Xiong, J. E. Laaser, P. Paoprasert, R. A. Franking, R. J. Hamers, P. Gopalan, and M. T. Zanni, *J. Am. Chem. Soc.*, 2009, **131**, 18040–18041.

26. A. G. Thomas and K. L. Syres, *Chem. Soc. Rev.*, 2012, **41**, 4207–4217.

27. A. Mattsson, S. Hu, K. Hermansson, and L. Österlund, *J. Chem. Phys.*, 2014, **140**, 034705.

28. M. Xu, H. Noei, M. Buchholz, M. Muhler, C. Wöll, and Y. Wang, *Catal. Today*, 2012, **182**, 12–15.

29. A. Vittadini, A. Selloni, F. P. Rotzinger, and M. Gratzel, *J. Phys. Chem. B*, 2000, **104**, 1300–1306.

30. N. Martsinovich, F. Ambrosio, and A. Troisi, *Phys. Chem. Chem. Phys.*, 2012, **14**, 16668–16676.

31. J. Calbo, M. Pastore, E. Mosconi, E. Orti, and F. De Angelis, *Phys. Chem. Chem. Phys.*, 2014, **16**, 4709–4719.

32. M. Pastore and F. De Angelis, *J. Phys. Chem. Lett.*, 2013, **4**, 956–974.

33. F. Ambrosio, N. Martsinovich, and A. Troisi, *J. Phys. Chem. C*, 2012, **116**, 2622–2629.

34. N. Martsinovich and A. Troisi, *J. Phys. Chem. C*, 2011, **115**, 11781–11792.

35. J. E. Laaser, J. R. Christianson, T. A. Oudenhoven, Y. Joo, P. Gopalan, J. R. Schmidt, and M. T. Zanni, *J. Phys. Chem. C*, 2014, **118**, 5854–5861.

36. W. R. Duncan and O. V Prezhdo, *Annu. Rev. Phys. Chem.*, 2007, **58**, 143–184.

37. S. Manzhos, H. Segawa, and K. Yamashita, *Phys. Chem. Chem. Phys.*, 2012, **15**, 1141–1147.

38. Y. Tateyama, M. Sumita, Y. Ootani, K. Aikawa, R. Jono, L. Han, and K. Sodeyama, *J. Phys. Chem. C*, 2014, **118**, 16863–16871.

39. L. Kronik, *Surf. Sci. Rep.*, 1999, **37**, 1–206.

40. H. Tatsumi, A. Sasahara, and M. Tomitori, *J. Phys. Chem. C*, 2013, **117**, 10410–10416.

41. E. Mosconi, A. Selloni, and F. De Angelis, *J. Phys. Chem. C*, 2012, **116**, 5932 –5940.

42. F. De Angelis, S. Fantacci, and R. Gebauer, *J. Phys. Chem. Lett.*, 2011, **2**, 813–817.

43. C. L. Anfuso, R. C. Snoeberger, A. M. Ricks, W. Liu, D. Xiao, V. S. Batista, and T. Lian, *J. Am. Chem. Soc.*, 2011, **133**, 6922–6925.

44. G. Kresse and J. Hafner, *Phys. Rev. B*, 1993, **47**, 558–561.

45. G. Kresse and J. Hafner, *Phys. Rev. B*, 1994, **49**, 14251–14269.

46. G. Kresse and J. Furthmüller, *Phys. Rev. B*, 1996, **54**, 11169–11186.

47. G. Kresse and J. Furthmüller, *Comput. Mater. Sci.*, 1996, **6**, 15–50.

48. J. P. Perdew, K. Burke, and M. Ernzerhof, *Phys. Rev. Lett.*, 1996, **77**, 3865–3868.

49. J. P. Perdew, K. Burke, and M. Ernzerhof, *Phys. Rev. Lett.*, 1997, **78**, 1396.

50. P. E. Blöchl, *Phys. Rev. B*, 1994, **50**, 17953–17979.

51. G. Kresse and D. Joubert, *Phys. Rev. B*, 1999, **59**, 1758–1775.

52. W. Humphrey, A. Dalke, and K. Schulten, *J. Mol. Graph.*, 1996, **14**, 33–38.

53. S. R. Bahn and K. W. Jacobsen, *Comput. Sci. Eng.*, 2002, **4**, 56–66.

54. C. J. Howard, T. M. Sabine, and F. Dickson, *Acta Crystallogr. Sect. B*, 1991, **47**, 462–468.

55. E. Bitzek, P. Koskinen, F. Gähler, M. Moseler, and P. Gumbsch, *Phys. Rev. Lett.*, 2006, **97**, 170201.

56. D. M. Newns, *Phys. Rev.*, 1969, **178**, 1123.

57. J. P. Muscat and D. M. Newns, *Prog. Surf. Sci.*, 1978, **9**, 1–43.

58. B. D. Dunnington and J. R. Schmidt, *J. Chem. Theory Comput.*, 2012, **8**, 1902–1911.

59. X. Pan, M.-Q. Yang, X. Fu, N. Zhang, and Y.-J. Xu, *Nanoscale*, 2013, **5**, 3601–3614.

60. X. Jiang, Y. Zhang, and J. Jiang, *J. Phys. Chem. C*, 2012, **116**, 22619–22624.

61. R. Schaub, E. Wahlström, A. Rønnau, E. Lagsgaard, I. Stensgaard, and F. Besenbacher, *Science*, 2003, **299**, 377–379.

62. Y. Joo, J. W. Spalenka, K. M. McElhinny, S. K. Schmitt, P. G. Evans, and P. Gopalan, *Langmuir*, 2014, **30**, 6104–6113.

63. R. A. Marcus, *J. Chem. Phys.*, 1956, **24**, 966.

64. R. A. Marcus, *Annu. Rev. Phys. Chem.*, 1964, **15**, 155–196.

65. M. Sumita, K. Sodeyama, R. Jono, L. Han, and Y. Tateyama, *Chem. Phys. Lett.*, 2013, **556**, 225–229.

66. R. J. Berry, D. Rigby, D. Duan, and M. Schwartz, *J. Phys. Chem. A*, 2006, **110**, 13–19.

67. M. Bixon and J. Jortner, *Russ. J. Electrochem.*, 2003, **39**, 3–8.

68. R. P. Domingue and M. D. Fayer, *J. Phys. Chem.*, 1986, **90**, 5141–5146.

69. J. Tang and S.-H. Lin, *Phys. Rev. E*, 2006, **73**, 061108.

*Theoretical Chemistry Institute and Department of Chemistry, University of Wisconsin-Madison, Madison, Wisconsin 53706, United States
Email: schmidt@chem.wisc.edu

†Electronic supplementary information (ESI) available.

Table of Contents Entry:

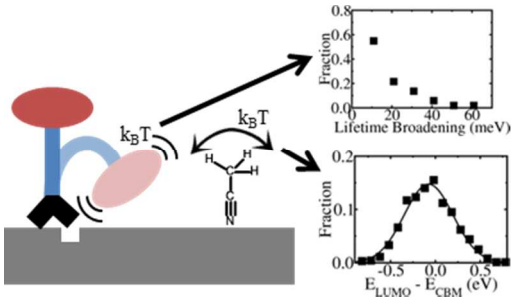

Structural heterogeneity, solvation, and thermal fluctuations all contribute to multiple dye-semiconductor charge injection rates.